Supplemental Information for

Polymorphic phase engineering of flat plasmons in a correlated oxide

Yangyu Zhu,†[a] Xuejin Zhang,†[a] Jaeseok Son,[b] Tae Won Noh,[b] Haohai Yu,[c] Huaijin Zhang,[c] Mingwen Zhao,*[a] and Yangyang Li*[a,c]

Affiliations

[a]School of Physics, Shandong University, Jinan 250100, China

[b]Department of Physics and Astronomy, Seoul National University, Seoul 08826, Republic of Korea

[c]State Key Laboratory of Crystal Materials and Institute of Crystal Materials, Shandong University, Jinan 250100, Shandong, China

† These authors contributed equally to this work.

*Authors to whom correspondence should be addressed: zmw@sdu.edu.cn and yangyang.li@sdu.edu.cn

Supplementary Methods

Fabrication of Ti_2O_3 epitaxial films

All Ti_2O_3 films were deposited on Al_2O_3 single-crystal substrates via pulsed laser deposition (PLD), employing a 248 nm Laser (KrF, Coherent). The films' thickness is approximately 300 nm. α-, o- and g-Ti_2O_3 films were deposited on (0001) Al_2O_3 substrates at temperatures of 600 °C 800 °C, and 950 °C, respectively. The PLD chamber was maintained at a pressure lower than 3.0×10^{-6} Torr. The laser's energy density was consistently set at ~2 J cm^{-2} for α-Ti_2O_3 and o-Ti_2O_3, while that for g-Ti_2O_3 is ~3 J cm^{-2}. The same corundum α-Ti_2O_3 target (Sigma-Aldrich 99.99%) was utilized for all films' growth.

Structural characterizations

XRD patterns were acquired using a Bruker D8 DISCOVER high-resolution diffractometer, equipped with Cu Kα radiation source and LynxEye detector. During the measurements, the diffractometer was operated at 35 kV and 50 mA at room temperature.

Spectroscopic ellipsometry measurements

The ellipsometry parameters, Ψ (the ratio of the amplitude of p- and s-polarized reflected light) and Δ (the phase difference between p- and s-polarized reflected light), were measured using a spectroscopic ellipsometer with a photon range of ~0.5 – 4 eV with incident angles of 60°, 65°, and 70°, at room temperature. The optical conductivity of Ti_2O_3 films was determined from the Ψ and Δ parameters, employing an air/Ti_2O_3/Al_2O_3 multilayer model, where the Ti_2O_3 films were assumed to be average, homogeneous, and uniform mediums.

Electronic transport measurements

The electronic transport properties of the Ti_2O_3 films were measured in a commercial Quantum Design physical property measurement system (PPMS). The resistivity and Hall effect measurements were conducted using the Van der Pauw geometry, with the samples sized at 5 × 5 mm. Aluminium wires were employed to establish connections between the samples and the PPMS puck.

Theoretical calculations

To further investigate the optical properties of Ti_2O_3 polymorphs, we calculated their dielectric constants. In solids, optical properties can be characterized by the complex dielectric function tensor. In general, the dielectric function can be regarded as the contribution of two parts, namely the intra-band part $\varepsilon(\omega)_{\alpha\beta}^{intra}$ described by the Drude model and the inter-band part $\varepsilon(\omega)_{\alpha\beta}^{inter}$ due to interband transitions. In this case, $Im\,\varepsilon$ of the interband contribution can be calculated by the interband transitions, while $Re\,\varepsilon$ of the interband contribution can be given by the Kramers-Kronig relation.[1] Therefore, the dielectric function can be expressed by[2]

$$\varepsilon(\omega)_{\alpha\beta} = 1 - \frac{\omega_{p,\alpha\beta}^2}{(\omega + i\gamma\omega)^2} + \varepsilon(\omega)_{\alpha\beta}^{inter},$$

where $\omega_{p,\alpha\beta}$ is the plasma frequency and γ is the lifetime broadening which is the reciprocal of the excited-state lifetime.

First-principles calculations were performed using density functional theory, as implemented in the Vienna ab simulation package (VASP)[3] and GPAW code,[4] both of which employ the projected augmented-wave method to model interactions between electrons and ions.[5] We utilized the Generalized Gradient Approximation (GGA) with the Perdew-Burke-Ernzerhof (PBE) function[6] for the exchange-correlation. The plane-wave energy cutoff was set to 500 eV. The GGA+U

method[7] was employed to address strong electron-electron correlations between the partially filled 3*d*-shells of Ti. The Hubbard interaction U_{eff} (U-J) was set to 2.2, 2.9, and 2.2 eV for α-Ti_2O_3, o-Ti_2O_3, and g-Ti_2O_3, respectively, based on the previous studies[1,8] and the experimental dielectric constants. Structure relaxation and electronic properties were calculated using VASP with the Monkhorst-Pack (MP) k-points grids of 8×8×8, 4×9×10, 4×12×4 for α-Ti_2O_3, o-Ti_2O_3, and g-Ti_2O_3, respectively. Structural optimization of the lattice constants and atomic positions was performed through total energy minimization. The optimization converged when the residual forces on each atom fell below 0.01 eV/Å and the total energy difference between successive iterations was less than 10^{-6} eV. The dynamic dielectric function and loss function were calculated using the GPAW code based on linear response theory.[9] The denser k-points grids of 31×31×31, 15×27×33, and 15×45×15 were adopted to converge the optical calculations. Under random phase approximation, the **q**-dependent dynamic dielectric function can be calculated by:

$$\varepsilon_{G,G'}^{RPA}(\mathbf{q},\omega) = \delta_{G,G'} - \frac{4\pi}{|\mathbf{q}+\mathbf{G}|^2}\chi_{G,G'}^{0}(\mathbf{q},\omega)$$

where $\chi_{G,G'}^{0}(\mathbf{q},\omega)$ is the non-interacting density response function in reciprocal space, which can be written as[10,11]

$$\chi_{\mathbf{GG'}}^{0}(\mathbf{q},\omega) = \frac{1}{\Omega}\sum_{\mathbf{k}}^{\mathrm{BZ}}\sum_{n,n'}\frac{f_{n\mathbf{k}} - f_{n'\mathbf{k}+\mathbf{q}}}{\omega + \varepsilon_{n\mathbf{k}} - \varepsilon_{n'\mathbf{k}+\mathbf{q}} + i\eta}\left\langle \psi_{n\mathbf{k}} \left| e^{-i(\mathbf{q}+\mathbf{G})\cdot\mathbf{r}} \right| \psi_{n'\mathbf{k}+\mathbf{q}} \right\rangle_{\Omega_{\mathrm{Cell}}} \left\langle \psi_{n\mathbf{k}} \left| e^{i(\mathbf{q}+\mathbf{G'})\cdot\mathbf{r}'} \right| \psi_{n'\mathbf{k}+\mathbf{q}} \right\rangle_{\Omega_{\mathrm{Cell}}}$$

where **q** stands for the Bloch vector of the incident wave and **G (G')** are reciprocal lattice vectors. $f_{n\mathbf{k}}$ is the Fermi-Dirac distribution function given by

$$f(E) = \frac{1}{1+\exp[(E-E_F)/k_BT]}$$

The Kohn-Sham energy eigenvalues, the wave function and the Fermi-Dirac distribution function for the nth band at wave vector k were obtained from the ground-state calculations. The

electron energy loss spectrum can be obtained from the macroscopic dielectric matrix defined by

$$\epsilon_M(q,\omega) = \frac{1}{\epsilon^{-1}_{00}}(q,\omega)$$

$$EELS = -\,Im\frac{1}{\epsilon_M(q,\omega)}$$

The plasmon energy was determined by identifying the peak positions in the EELS. A broadening parameter of 0.05 eV was applied when calculating the spectra. The plane wave basis set with a cutoff energy of 50 eV was used to describe the local field effect (LFE). The irreducible representations and parity of the electronic states were computed using the Irvsp code.[12]

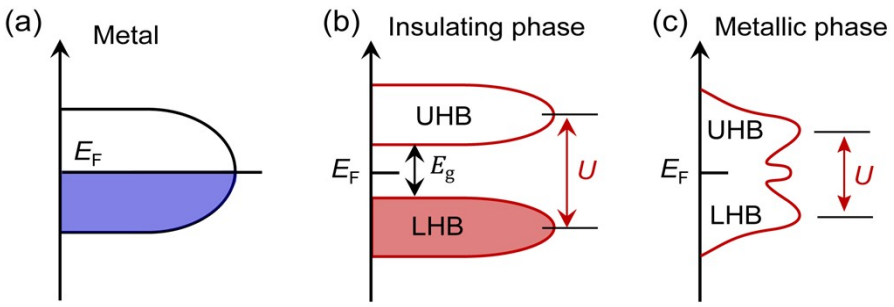

Fig. S1. Schematic band structures of metal and Mott insulator. (a) Schematic electronic structure of a conventional metal. (b) (c) Schematic electronic structure of a Mott insulator in the insulating and metallic phases, respectively.

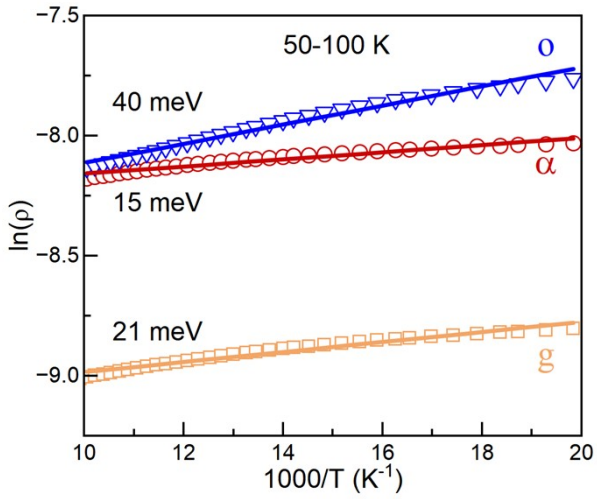

Fig. S2. ln(ρ) vs 1/T dependencies at the range of 50–100 K, fitted from the data in Fig. 2(d).

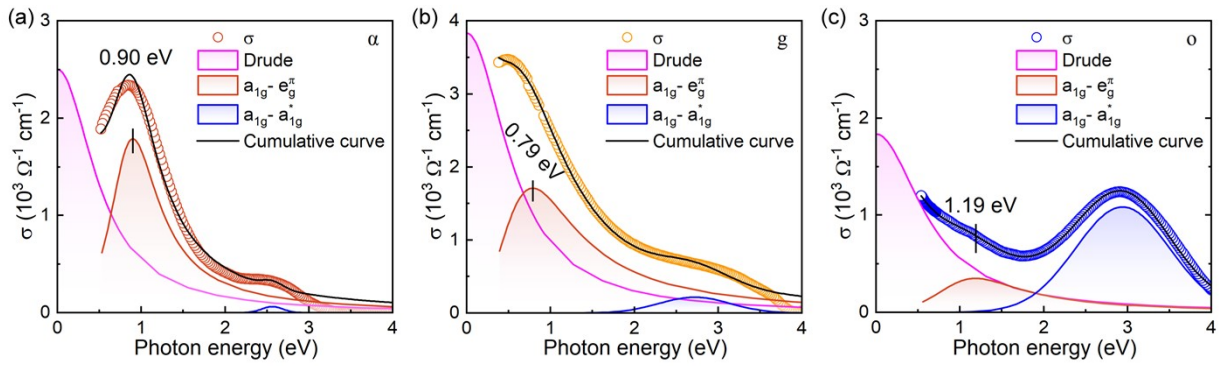

Fig. S3. Peak fitting of optical conductivity for Ti_2O_3 polymorphs. (a): α-Ti_2O_3**.** (b): o-Ti_2O_3**.** (c): g-Ti_2O_3. The red, blue, and dark grey lines correspond to the $a_{1g} - e_g^{\pi}$, $a_{1g} - a_{1g}^{*}$ interband transitions and cumulative curves, respectively.

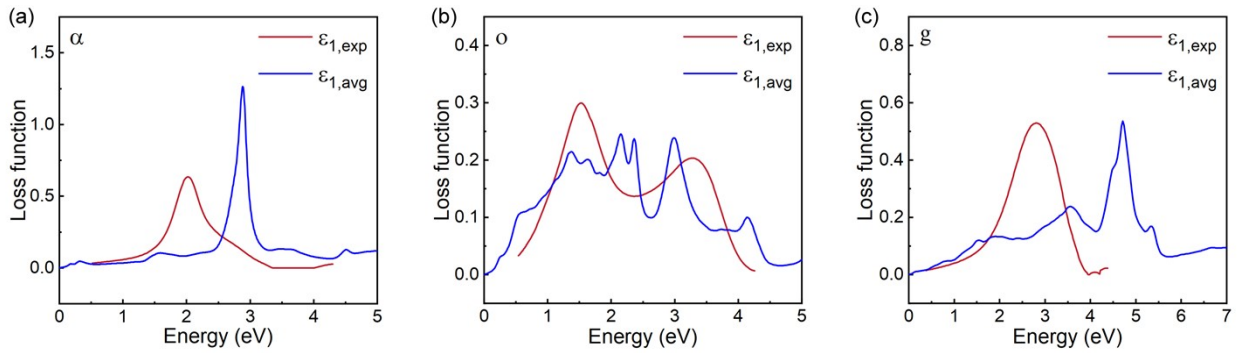

Fig. S4. Comparison of EELS from ellipsometry data (red lines) and effective average of $q \sim 0$ DFT data (blue lines) from all directions for (a) α-, (b) o-, and (c) g-Ti_2O_3.

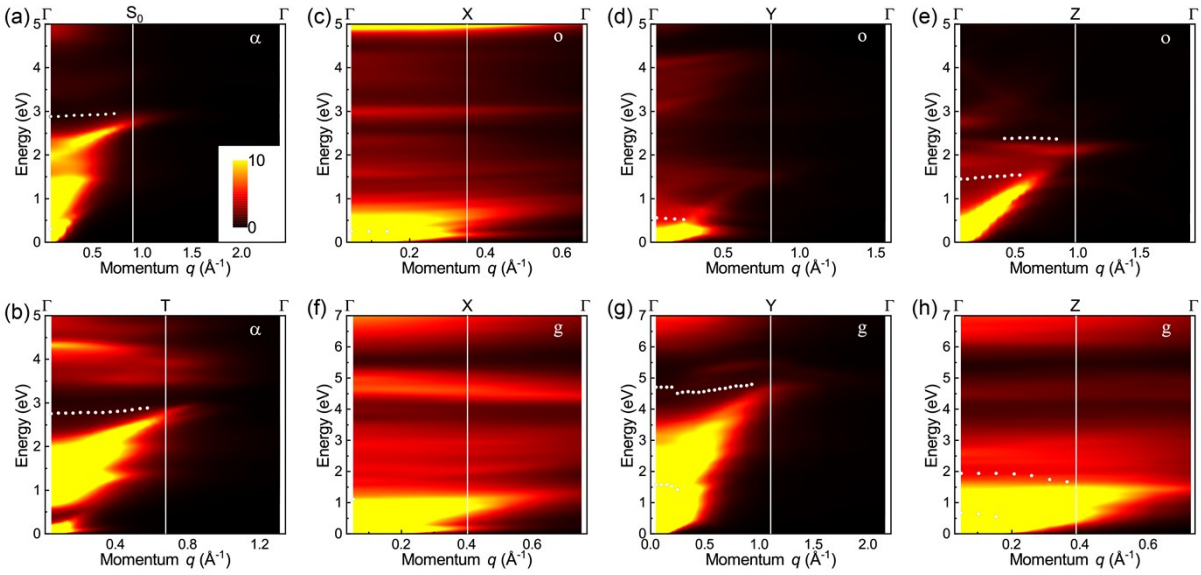

Fig. S5. Imaginary part of dynamic dielectric function ε(q, ω) in Ti_2O_3 polymorphs. Calculated dielectric function spectra with local field effects (LFE) for Ti_2O_3 polymorphs along different crystal directions. (a) and (b) α-Ti_2O_3 along in-plane (Γ-S_0) and out-of-plane (Γ-T) directions. (c)-(h) o- and g- Ti_2O_3 along the x-, y- and z-directions. The points in the figure are extracted from the peaks of the EELS spectra, representing the energy of plasmons. The data points inside the black area correspond to plasmons with low damping.

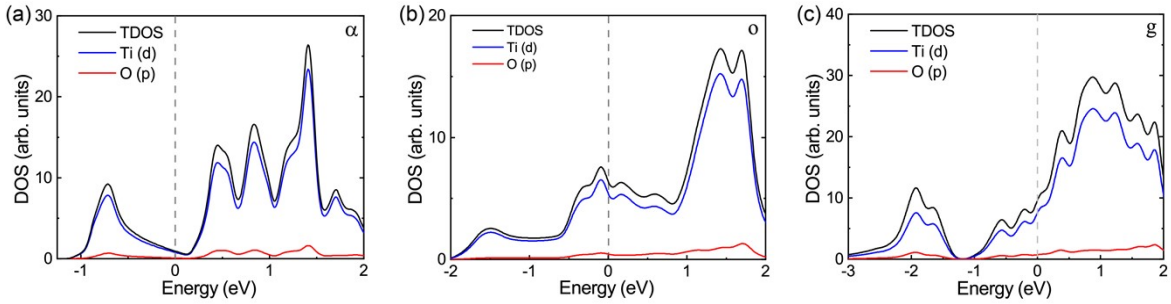

Fig. S6. Projected density of states (PDOS) for Ti_2O_3 polymorphs. (a): α-Ti_2O_3**.** (b): o-Ti_2O_3**.** (c): g-Ti_2O_3. The black, blue, and red lines correspond to the total DOS, Ti 3*d* states, and O 2*p* states, respectively.

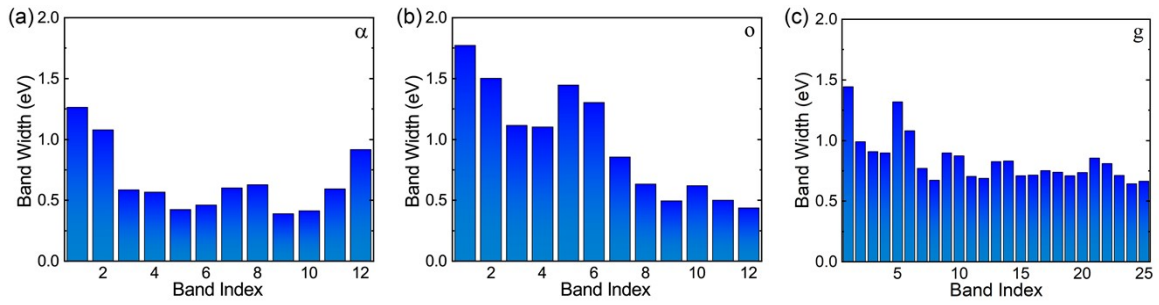

Fig. S7. Bandwidths of Ti_2O_3 polymorphs. (a): α-Ti_2O_3**.** (b): o-Ti_2O_3**.** (c): g-Ti_2O_3. The blue bar graphs visually present the bandwidth values, facilitating comparison between the three Ti_2O_3 polymorphs.

Table S1. The parity (even/odd) of the different band states at the Γ point in α-Ti_2O_3 is denoted by + for even and - for odd. It indicates possible interband transitions between bands based on selection rules. The ticks (√) mark allowed transitions from lower to higher energy bands requiring a change in parity.

Band index	Occupation	Parity	Transition from band 1	Transition from band 2
1	Filled	+		
2	Half-filled	+		
3	Empty	+		
4	Empty	-	√	√(main)
5	Empty	+		
6	Empty	+		
7	Empty	-	√	√
8	Empty	-	√	√
9	Empty	-	√	√
10	Empty	-	√	√
11	Empty	-	√	√
12	Empty	+		

Table S2. The transition dipole moments (TDMs) between electronic states in α-Ti_2O_3 at the Γ point. The square of TDM $|\langle\Psi_m|r|\Psi_n\rangle|^2$ and its components (X: $|\langle\Psi_m|x|\Psi_n\rangle|^2$, Y: $|\langle\Psi_m|y|\Psi_n\rangle|^2$, and Z: $|\langle\Psi_m|z|\Psi_n\rangle|^2$) are shown for each transition process, respectively. + and – denote the even and odd parity of the electric states, respectively. Transition between states of same parity is forbidden.

TDM2 (Debye2) / Transition	X-component	Y-component	Z-component	Total
1(+)→3(+)	0	0	0	0
1(+)→4(-)	0	0	0	0
2(+)→4(-)	1.429×10^6	1.987×10^7	1.060×10^7	3.190×10^7
1(+)→5(+)	0	0	0	0
2(+)→5(+)	0	0	0	0
1(+)→6(+)	0	0	0	0
2(+)→6(+)	0	0	0	0
1(+)→7(-)	0.499	6.826	3.530	10.856
2(+)→7(-)	5.319	55.529	29.442	90.291
1(+)→8(-)	0.628	1.139	3.319	5.086
2(+)→8(-)	646.650	6.215	37.693	690.558
1(+)→9(-)	1.119	2.250	5.950	9.388
2(+)→9(-)	260.919	0.287	26.845	288.051
1(+)→10(-)	0.893	12.456	6.696	20.045
2(+)→10(-)	0.360	2.731	3.137	9.229
1(+)→11(-)	16.0425	0.013	2.628	18.684
2(+)→11(-)	3.639	6.842	18.405	28.887
1(+)→12(+)	0	0	0	0

2(+)→12(+)	0	0	0	0

Table S3. The parity (even/odd) of the different band states at the Γ point in o-Ti_2O_3 is denoted by + for even and - for odd. It indicates possible interband transitions between bands based on selection rules. The ticks (√) mark allowed transitions from lower to higher energy bands requiring a change in parity.

Band index	Occupation	Parity	Transition from band 1	Transition from band 2	Transition from band 3
1	Filled	+			
2	Filled	+			
3	Half-filled	+			
4	Empty	-	√	√	√
5	Empty	+			
6	Empty	-	√	√	√(main)
7	Empty	-	√	√	√
8	Empty	-	√	√	√
9	Empty	-	√	√	√
10	Empty	+			
11	Empty	-	√	√	√
12	Empty	+			

Table S4. The transition dipole moments (TDMs) between electronic states in o-Ti_2O_3 at the Γ point. The square of TDM $|\langle\Psi_m|r|\Psi_n\rangle|^2$ and its components (X: $|\langle\Psi_m|x|\Psi_n\rangle|^2$, Y: $|\langle\Psi_m|y|\Psi_n\rangle|^2$, and Z: $|\langle\Psi_m|z|\Psi_n\rangle|^2$) are shown for each transition process, respectively. + and – denote the even and odd parity of the electric states, respectively. Transition between states of same parity is forbidden.

TDM² (Debye²) / Transition	X-component	Y-component	Z-component	Total
1(+)→3(+)	0	0	0	0
2(+)→3(+)	0	0	0	0
1(+)→4(-)	0	0	0	0
2(+)→4(-)	0	0	0	0
3(+)→4(-)	0	0	0	0
1(+)→5(+)	0	0	0	0
2(+)→5(+)	0	0	0	0
3(+)→5(+)	0	0	0	0
1(+)→6(-)	0	0	0	0
2(+)→6(-)	0	32.793	0	32.793
3(+)→6(-)	0	0	333.013	333.013
1(+)→7(-)	0	3.669	0	3.669
2(+)→7(-)	0	0	0	0
3(+)→7(-)	0	0	0	0
1(+)→8(-)	0	0	0	0
2(+)→8(-)	0	0	0	0
3(+)→8(-)	15.628	0	0	15.628
1(+)→9(-)	54.902	0	0	54.902
2(+)→9(-)	0	0	0	0
3(+)→9(-)	0	0	0	0

1(+)→10(+)	0	0	0	0
2(+)→10(+)	0	0	0	0
3(+)→10(+)	0	0	0	0
1(+)→11(-)	0	0	0	0
2(+)→11(-)	0	0	0	0
3(+)→11(-)	0	0	0	0
1(+)→12(+)	0	0	0	0
2(+)→12(+)	0	0	0	0
3(+)→12(+)	0	0	0	0

Table S5. The parity (even/odd) of the different band states at the Γ point in g-Ti_2O_3 is denoted by + for even and - for odd. It indicates possible interband transitions between bands based on selection rules. The ticks (√) mark allowed transitions from lower to higher energy bands requiring a change in parity.

Band index	Occupation	Parity	Transition from band 1	Transition from band 2	Transition from band 3	Transition from band 4
1	Filled	-				
2	Filled	+				
3	Filled	+				
4	Filled	-				
5	Filled	+				
6	Half-filled	-		√	√	
7	Half-filled	+	√			√
8	Half-filled	-		√	√	
9	Half-filled	+	√(main)			√
10	Half-filled	-		√	√(main)	
11	Empty	-		√	√	
12	Empty	-		√	√	
13	Empty	+	√			√(main)
14	Empty	-		√	√	
15	Empty	+	√			√
16	Empty	-		√	√	
17	Empty	+	√			√
18	Empty	+	√			√
19	Empty	+	√			√

20	Empty	-			√	√	
21	Empty	-			√(main)	√	
22	Empty	-			√	√	
23	Empty	+	√				√
24	Empty	-			√	√	
25	Empty	-			√	√	
26	Empty	+	√				√
27	Empty	+	√				√
28	Empty	+	√				√

Table S6. The transition dipole moments (TDMs) between electronic states in g-Ti_2O_3 at the Γ point. The square of TDM $|\langle\Psi_m|r|\Psi_n\rangle|^2$ and its components (X: $|\langle\Psi_m|x|\Psi_n\rangle|^2$, Y: $|\langle\Psi_m|y|\Psi_n\rangle|^2$, and Z: $|\langle\Psi_m|z|\Psi_n\rangle|^2$) are shown for each transition process, respectively. + and – denote the even and odd parity of the electric states, respectively. Transition between states of same parity is forbidden.

TDM² (Debye²) / Transition	X-component	Y-component	Z-component	Total
1(-)→6(-)	0	0	0	0
2(+)→6(-)	13.291	0	0	13.291
3(+)→6(-)	0	0	98.887	98.887
4(-)→6(-)	0	0	0	0
1(-)→7(+)	11.622	0	0	11.622
2(+)→7(+)	0	0	0	0
3(+)→7(+)	0	0	0	0
4(-)→7(+)	0	0	18.867	18.867
1(-)→8(-)	0	0	0	0
2(+)→8(+)	0	0	0	0
3(+)→8(+)	2.746	0	0	2.746
4(-)→8(-)	0	0	0	0
1(-)→9(+)	0	14.014	0	14.014
2(+)→9(+)	0	0	0	0
3(+)→9(+)	0	0	0	0
4(-)→9(-)	0	0	0	0
1(-)→10(-)	0	0	0	0
2(+)→10(-)	0.062	0	0	0.062
3(+)→10(-)	0	24.369	0	24.369
4(-)→10(-)	0	0	0	0

1(-)→11(-)	0	0	0	0
2(+)→11(-)	18.371	0	0	18.371
3(+)→11(-)	0	0	2.216	2.216
4(-)→11(-)	0	0	0	0
1(-)→12(-)	0	0	0	0
2(+)→12(-)	0	0	7.493	7.493
3(+)→12(-)	0.002	0	0	0.002
4(-)→12(-)	0	0	0	0
1(-)→13(+)	0	0	0	0
2(+)→13(+)	0	0	0	0
3(+)→13(+)	0	0	0	0
4(-)→13(+)	0	22.419	0	22.419
1(-)→14(-)	0	0	0	0
2(+)→14(-)	2.922	0	0	2.922
3(+)→14(-)	0	0	0.012	0.012
4(-)→14(-)	0	0	0	0
1(-)→15(+)	0	0	3.707	3.707
2(+)→15(+)	0	0	0	0
3(+)→15(+)	0	0	0	0
4(-)→15(+)	5.332	0	0	5.332
1(-)→16(-)	0	0	0	0
2(+)→16(-)	0	0	3.313	3.313
3(+)→16(-)	13.880	0	0	13.880
4(-)→16(-)	0	0	0	0
1(-)→17(+)	0	0.479	0	0.479
2(+)→17(+)	0	0	0	0
3(+)→17(+)	0	0	0	0

4(-)→17(+)	0	0	0	0
1(-)→18(+)	1.641	0	0	1.641
2(+)→18(+)	0	0	0	0
3(+)→18(+)	0	0	0	0
4(-)→18(+)	0	0	0.013	0.013
1(-)→19(+)	0.511	0	0	0.511
2(+)→19(+)	0	0	0	0
3(+)→19(+)	0	0	0	0
4(-)→19(+)	0	0	4.258	4.258
1(-)→20(-)	0	0	0	0
2(+)→20(-)	0.062	0	0	0.062
3(+)→20(-)	0	0	17.187	17.187
4(-)→20(-)	0	0	0	0
1(-)→21(-)	0	0	0	0
2(+)→21(-)	0	7.983	0	7.983
3(+)→21(-)	0	0	0	0
4(-)→20(-)	0	0	0	0
1(-)→22(-)	0	0	0	0
2(+)→22(-)	0	0	0	0
3(+)→22(-)	0	1.028	0	1.028
4(-)→22(-)	0	0	0	0
1(-)→23(+)	0	0	0.0001	0.0001
2(+)→23(+)	0	0	0	0
3(+)→23(+)	0	0	0	0
4(-)→23(+)	2.748	0	0	2.748
1(-)→24(-)	0	0	0	0
2(+)→24(-)	0	1.489	0	1.489

3(+)→24(+)	0	0	0	0
4(-)→24(-)	0	0	0	0
1(-)→25(-)	0	0	0	0
2(+)→25(-)	0	0	1.047	1.047
3(+)→25(-)	2.874	0	0	2.874
4(-)→25(-)	0	0	0	0
1(-)→26(+)	0.020	0	0	0.020
2(+)→26(+)	0	0	0	0
3(+)→26(+)	0	0	0	0
4(-)→26(+)	0	0	3.091	3.091
1(-)→27(+)	0	0	0.094	0.094
2(+)→27(+)	0	0	0	0
3(+)→27(+)	0	0	0	0
4(-)→27(+)	0.460	0	0	0.460
1(-)→28(+)	0	0	0	0
2(+)→28(+)	0	0	0	0
3(+)→28(+)	0	0	0	0
4(-)→28(+)	0	0.142	0	0.142

References

1 N. Hasegawa, K. Yoshimatsu, D. Shiga, T. Kanda, S. Miyazaki, M. Kitamura, K. Horiba and H. Kumigashira, *Phys. Rev. B*, 2022, **105**, 235137.

2 S. M. Sze, Y. Li and K. K. Ng, *Physics of semiconductor devices*, John wiley & sons, 2021.

3 G. Kresse and J. Furthmüller, *Phys. Rev. B*, 1996, **54**, 11169-11186.

4 J. Enkovaara, C. Rostgaard, J. J. Mortensen, J. Chen, M. Dułak, L. Ferrighi, J. Gavnholt, C. Glinsvad, V. Haikola, H. A. Hansen, H. H. Kristoffersen, M. Kuisma, A. H. Larsen, L. Lehtovaara, M. Ljungberg, O. Lopez-Acevedo, P. G. Moses, J. Ojanen, T. Olsen, V. Petzold, N. A. Romero, J. Stausholm-Møller, M. Strange, G. A. Tritsaris, M. Vanin, M. Walter, B. Hammer, H. Häkkinen, G. K. H. Madsen, R. M. Nieminen, J. K. Nørskov, M. Puska, T. T. Rantala, J. Schiøtz, K. S. Thygesen and K. W. Jacobsen, *J. Phys.: Condens. Matter*, 2010, **22**, 253202.

5 P. E. Blöchl, *Phys. Rev. B*, 1994, **50**, 17953-17979.

6 J. P. Perdew, K. Burke and M. Ernzerhof, *Phys. Rev. Lett.*, 1996, **77**, 3865-3868.

7 I. A. Vladimir, F. Aryasetiawan and A. I. Lichtenstein, *J. Phys.: Condens. Matter*, 1997, **9**, 767.

8 Y. Li, Z. G. Yu, L. Wang, Y. Weng, C. S. Tang, X. Yin, K. Han, H. Wu, X. Yu, L. M. Wong, D. Wan, X. R. Wang, J. Chai, Y.-W. Zhang, S. Wang, J. Wang, A. T. S. Wee, M. B. H. Breese, S. J. Pennycook, T. Venkatesan, S. Dong, J. M. Xue and J. Chen, *Nat. Commun.*, 2019, **10**, 3149.

9 J. Yan, J. J. Mortensen, K. W. Jacobsen and K. S. Thygesen, *Phys. Rev. B*, 2011, **83**, 245122.

10 S. L. Adler, *Phys. Rev.*, 1962, **126**, 413-420.

11 N. Wiser, *Phys. Rev.*, 1963, **129**, 62-69.

12 J. Gao, Q. Wu, C. Persson and Z. Wang, *Comput. Phys. Commun.*, 2020, **261**, 107760.